Hindawi
Geofluids
Volume 2021, Article ID 8092331, 18 pages
https://doi.org/10.1155/2021/8092331

Research Article

Nanoconfined Water in Shales and Its Impact on Real Gas Flow

Yudan Li,[1,2] **Shaohua Gu**,[1,2] **and Cheng Dai**[1,2]

[1]*Petroleum Exploration & Production Research Institute, Sinopec, Beijing 102206, China*
[2]*State Key Laboratory of Shale Oil and Gas Enrichment Mechanisms and Effective Development, Shahe, Beijing 102206, China*

Correspondence should be addressed to Yudan Li; dandancup@163.com

Received 25 April 2021; Accepted 28 July 2021; Published 16 August 2021

Academic Editor: Yonghui Wu

The presence of water, i.e., connate or hydraulic fracturing water, along with the gaseous hydrocarbons in shale nanopores is largely overlooked by previous studies. In this work, a new unified real gas-transport model has been developed for both organic and inorganic porous media accounting for the nanoconfined water film flow. More specifically, a gas core flows in the center of the organic/inorganic pore surrounded by a water film which can be further divided into an interfacial region (near-wall water) and bulk region (bulk water). We differentiate the varying water viscosity between the two regions and consider disparate slip boundaries; that is, the near-wall water can slip along the hydrophobic organic pore surface while it is negligible in hydrophilic inorganic pores. Incorporating modified boundary conditions into the Navier-Stokes equations, gas transport model through single organic/inorganic pore is derived. The model is also comprehensively scaled up to the porous media scale considering the porosity, tortuosity, and total organic carbon (TOC) contents. Results indicate that the gas flow capacity decreases in moist conditions with mobile or nonmobile water film. A mobile water film, however, compensates its negative effect up to 50% by enhancing gas flow compared with static water molecules. The real gas flow is dominated by the gas slippage and water film mobility which are dependent upon pore-scale parameters such as pore sizes, topology, pressure, and surface wettability. Compared with inorganic pores, gas transport in organic pores is greatly enhanced by the water film flow due to the strong water slip. Moreover, the contribution of water film mobility is remarkable in small pores with large contact angles, especially at high pressures. At moist conditions, the real gas effect enhances gas flow by improving both gas slippage and water film mobility, which is more prominent in smaller pores at high pressures. The presented model and its results will further advance our understanding of the mechanisms responsible for the water and gas transport in nanoporous media, and consequently, the hydrocarbon exploration of shale reservoirs.

1. Introduction

Shale gas, which predominantly consists of methane, plays an increasingly important role in global gas production due to its low emissions, high energy efficiency, and abundant reserves in the world [1]. Horizontal well drilling combined with multistage hydraulic fracturing has enabled economic developments of the shale gas resources [2]. The initial and/or injected water can coexist with methane at pore levels creating multiphase pore fluid occupancies of gas and water in the nanopores of shale formations [3, 4]. As a result, a better understanding of the multiphase flow of gas and water within shale nanopores is particularly important for gas production from shales and carbon dioxide sequestration processes.

The X-ray diffraction mineralogy analysis results show that the typically heterogeneous shale contains various proportions of the organic matter (OM) and inorganic matrix (iOM) [5]. The majority of pores are nanopores ranging from a few nanometers to several hundred nanometers [6]. Such wide pore size distributions complicate gas storage and transport properties of shales. In particular, small pore sizes of shales are comparable to the mean free path (MFP) of the producing gas. And as a result, molecular collisions with the grain surface should be taken into account in addition to the intermolecular collisions [7, 8]. The Knudsen number (K_n), defined as the ratio of the molecular MFP to a characteristic length (e.g., pore diameter/aperture), is often used to represent the relative collisions of gas molecules to each other versus the pore walls [9]. Based on the K_n values, free

gas transport mechanisms can be classified into continuum ($K_n < 10^{-3}$), slip ($10^{-3} < K_n < 10^{-1}$), transition ($10^{-1} < K_n < 10$), and free molecular ($K_n > 10$) flow regimes [10]. Under reservoir conditions, the K_n generally ranges from 2×10^{-4} to 6, which means continuum, slip, and transition flow regimes can coexist for the transport mechanisms of gas in nanopores [11]. Researchers have used a wide range of experimental, analytical, and simulation methods to better understand mechanisms responsible for the gaseous methane transport through nanoporous shale samples. Moghaddam and Jamiolahmady [8] studied slip flow in shales by measuring slip permeability of shale core samples and reported that the slip coefficient in porous media is higher than those in nonporous systems due to greater surface area and roughness. Wang et al. [12] developed an alternative approach by combining experimental and mathematical methods to estimate the permeability of tight porous media. They pointed out that a simple experimental method is not always reliable especially when the pressure is high or the pore sizes are small. Most of these methods, however, are focused on dry samples. There is limited information on the gas slip flow characteristics for the nanopore fluid occupancies consisting of both water and gas. Accurate and reliable experimental measurement of the permeability is often challenging due to the extremely low permeability values. Therefore, other numerical methods such as the Lattice-Boltzmann (LBM), pore network (PN), and molecular dynamic (MD) have been used to simulate fluid flow at nanoscales [13–17]. These simulation techniques, however, are often excessively time-consuming and not applicable to the large-scale models due to the computational limitations and upscaling challenges [18]. Besides, the presence of water aggravates the simulation complexity further. Alternatively, it has been shown that the gas flow in micro- and nanochannels can be adequately described by solving the Navier-Stokes (N-S) equations with modified boundary conditions (i.e., 1st, 2nd, and 1.5 orders) for the slip and transition flow regimes [19, 20]. These studies have shown that the application of N-S equations with the velocity-slip boundary conditions is adequate for the modeling of gas flow.

It is worth to emphasize that the validity of the above discussion is limited to the single gas flow in nanopores. It is well known that shale is under moist conditions; for example, the moisture contents of kerogen from the Kuonamka Formation range from 0.6 to 5% [21, 22]. Based on the experimental analysis of core samples [23–25], the initial water saturation of Barnett, Marcellus, Haynesville, and Fayetteville Basins is 0.25-0.35, 0.12-0.35, 0.15-0.35, and 0.25-0.5, respectively. Moreover, field data indicates that during the hydraulic fracturing operation, thousands of cubic meters of fracturing fluid are forcibly injected into the subsurface reservoir, while only a small fraction of the injected fluid (as low as 10% or less are reported for some shale strata) can be recovered during the clean-up period [26]. Where has the water flown to? The loss of large volumes of fracturing fluid has created lots of concerns on the technology, economy, and environment [27]. A possible explanation of the observed high fluid loss during the injection period could be a liquid slip in the nanoscale pores of shales [28], and hence, the two-phase flow could occur in shale formations. Therefore, modeling and predicting gas transport behavior confined within nanopores under moist conditions are essential to accurately plan different stages of shale gas productions. To investigate multiphase flow at nanoscales, Wu et al. [29] proposed a new laboratory-on-chip approach for direct visualization of the fluid flow behavior in nanochannels. They investigated gas-to-water displacements in 100 nanochannels each 100 (nm) wide. Three types of flow patterns were observed; one of the three types of flow patterns is that gas is located in the middle of the nanochannels surrounded by water layers on the side walls. Chalmers and Bustin [30] compared a suite of moist shale samples and found that the moisture content plays a significant role in the methane sorption capacity depending on the distribution of hydrophobic and hydrophilic sites in pore networks. Later on, Zhao et al. [31] studied the impact of water contents on methane sorption capacity using MD and Monte Carlo (MC) simulations. Their results indicate that the gas adsorption capacity on the moist kerogen decreases with the increase in moist contents. Currently, the flow of nanoconfined water has attracted interests among researchers with different backgrounds spanning from water purification to the energy storage, conversion, and geophysical processes. Li et al. [32–34] quantified the water film thickness inside of a water-wet nanochannel based on the disjoining pressure and surface forces. Wu et al. [35] proposed a simple model for the flow of confined water based on the concept of effective slip. They reported that the flow capacity of nanoconfined water can range 10^{-1}-10^{7} times that calculated by the no-slip Hagen-Poiseuille equation for nanopores with various contact angles and dimensions. Later on, Sun et al. [36] established an analytical model for the conductance of confined water in the nanopores. They pointed out that the interaction between pore surface and fluid molecules plays a key role in the flow of water, especially for the nano-sized pores. It is worth emphasizing that the physical properties (e.g., viscosity and density) of water confined within the nanopores can drastically change resulting from water-wall interactions [36]. Thomas and McGaughey [37] and Wu et al. [35] divided the confined water into two parts, namely, bulk-like region and interface region with a fixed thickness of ~0.7 nm (i.e., two molecular layers). They assumed homogeneous physical properties for each region. Atomic-force microscopy and molecular simulations [38] indicate that there is a unique structural ordering of water confined in the hydrophilic channel wall, showing a sharp increase in the viscosity than that of the bulk water. Contrary to inorganic pores, organic pores are considered hydrophobic [32]. Moreover, since fluid flow in nanochannels is greatly affected by surface wettability, the conventional continuous flow with the no-slip assumption is no longer applicable in both hydrophobic (i.e., OM) and hydrophilic (i.e., iOM) pores [35]. Similar to gas slippage, water can also slip at the nanoscale, which is generally quantified by slip length, defined as a ratio of fluid flow velocity to the shear rate at the pore surface [36]. Based on previous studies, viscosity distribution and slip length need to be considered in analyzing confined water flow through nanopores.

In the gas shale reservoirs, the pore pressure is often very high. Especially in deep shale reservoirs, the pressure could be as high as 60 (MPa) such as the Sichuan Basin in China. Under these extreme conditions, the gas transport characteristics are significantly different than those of the laboratory conditions [39]. Nonetheless, many established models in the literature might lose the validity of the ideal-gas law because of the real-gas effect at high ambient pressures. Curtis [40] has summarized geological parameters for five representative shale-gas systems (Antrim, Ohio, New Albany, Barnett, and Lewis) in the US, with pressure from 2.0 to 28.0 (MPa) and temperature from 298 to 366 (K). Consequently, the shale-gas behavior cannot be described sufficiently by the ideal-gas law at such reservoir conditions. This is because at high pressure, due to a high gas density, a van der Waals force arising from gas molecules to molecules is notable, which is nonnegligible by affecting gas flow behavior. Moreover, the volume size of the gas molecule is nearly comparable to the scale of the nanopores, and it cannot be treated as a point [39, 41, 42]. Both of the factors are named as a real gas effect, which needs to be considered in order to accurately quantify the gas transport through shale porous media under reservoir conditions.

In this work, a new unified gas-transport model, accounting for the nanoconfined water flow, has been developed to characterize the real-gas flow in both organic and inorganic porous media. Considering various cross-section shapes of nanopores within the shale, the organic and inorganic pores are modelled as nanocapillaries and nanoslits with arbitrary aspect ratios, respectively. Moreover, a gas core filled the middle of the nanochannel surrounded by a water film which can be further divided into an interfacial region and bulk region. Meanwhile, the near-wall water can slip along the hydrophobic (i.e., OM) pore surface. We first derive the gas transport model through single nanocapillary/nanoslit based on N-S equations by combining modified boundary conditions. The model also extends to characterize the real-gas flow in a porous media (i.e., OM, iOM, and shale matrix) incorporating the porosity, tortuosity, and TOC contents. Subsequently, the proposed model is validated against experimental data and other models in the literature. Then, the AGP evolution at variable boundary conditions, the sensitivity of impact factors, and the contributions of gas slippage and water film mobility to gas flow in the new unified gas-transport model are implemented.

2. Model Development

Typically, the shale matrix is a dual-wettability porous system, characterized by oil-wetting or hydrophobic organic pores and water-wetting or hydrophilic inorganic pores [5]. Observed from SEM images, the majority of organic and inorganic nanopores have circular and slit type shapes, respectively [43, 44]. As such, gas flow mechanisms in organic and inorganic pores should be distinguished. In this section, gas transport models through OM and iOM incorporating gas slippage and water film mobility are established firstly; then, the AGP of shale matrix is obtained based on TOC contents. As we mentioned before, it is hard to describe the actual fluid distribution by practical mathematical expressions accurately. To address this issue, a well-developed simplification is made that the pore space of OM/iOM is hypothetically divided into three regions with homogeneous physical properties, i.e., free gas flow (central zone), bulk water flow (bulk region), and near-wall water flow (interfacial region) (Figures 1 and 2). Besides, some reasonable assumptions are made as follows:

(i) Single-phase methane and water flow in nanopores

(ii) The pore size difference within OM or iOM is neglected

(iii) There is no mass transfer between OM and iOM

(iv) The system is isothermal and homogeneous

2.1. Gas Flow Behavior through Hydrophobic Nanopores (OM). Molecular simulation results indicated that kerogen might have mixed-wet or even hydrophilic characteristics [45]. Moreover, the recent study [35] suggested that the near-wall water velocity is several orders larger than bulk water in hydrophobic nanopores with the contact angle larger than 90°. Because current two-phase flow experiment and methane-water molecular simulation data based on realistic organic matter (kerogen) model are not available, we assume that once water flows into the organic pore under a certain pressure drop, the gas will flow in the center of the pore while the water can slip fast along the surface wall. This assumption is physically valid, and our model can be viewed as the conceptual model to study gas-water flow pattern in nanoscale organic matter.

When the pore dimension is down to the nanoscale, the surface force becomes noticeable, which has a significant impact on the physical properties of the confined fluid. Based on Wu et al.

$$\mu_{\mathrm{wf}} = (-0.018\theta_{\mathrm{OM}} + 3.25)\mu_{\mathrm{wb}}. \tag{1}$$

[35], the water viscosity within an interfacial region is the function of a contact angle, defined as where μ_{wf} and μ_{wb} are the water viscosity within the interfacial and bulk region, respectively. θ_{OM} ranging from 90° to 180° is the contact angle of the organic pore.

The water film thickness h_c at different RHs inside single nanopore can be quantified as [33]

$$\Pi_c(h_c) = -\frac{\mathrm{RT}}{V_m} \ln \frac{P_v}{P^*}. \tag{2}$$

Noted that the thickness of the interfacial region (h_δ) always lies in a range of 0.5-1.5 (nm) [36].

Here, $\Pi_c(h_c)$ is the disjoining pressure, which is given as [33]

$$\Pi_c(h_c) = \frac{r_0}{r_0 - h_c}\Pi(h_c) + P_t = \frac{r_0}{r_0 - h_c}\Pi(h_c) + \frac{\gamma}{r_0 - h_c}, \tag{3}$$

where $\Pi(h_c)$ is the total disjoining pressure.

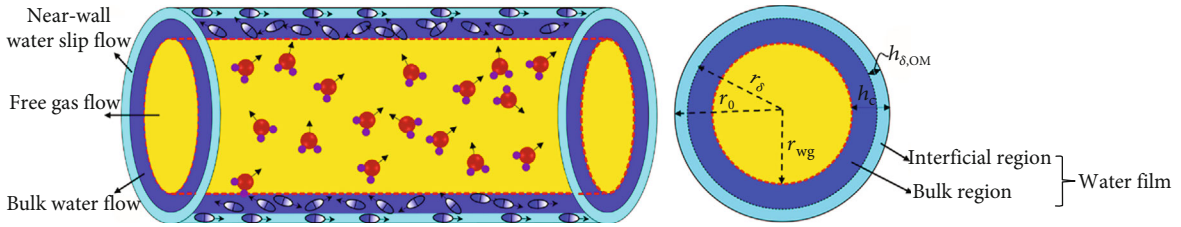

Figure 1: Illustration of the gas-water flow in nanoscale organic pores (viscous and slip flow of free gas in the pore center, viscous flow of bulk water, and the viscous and slip flow of near-wall water).

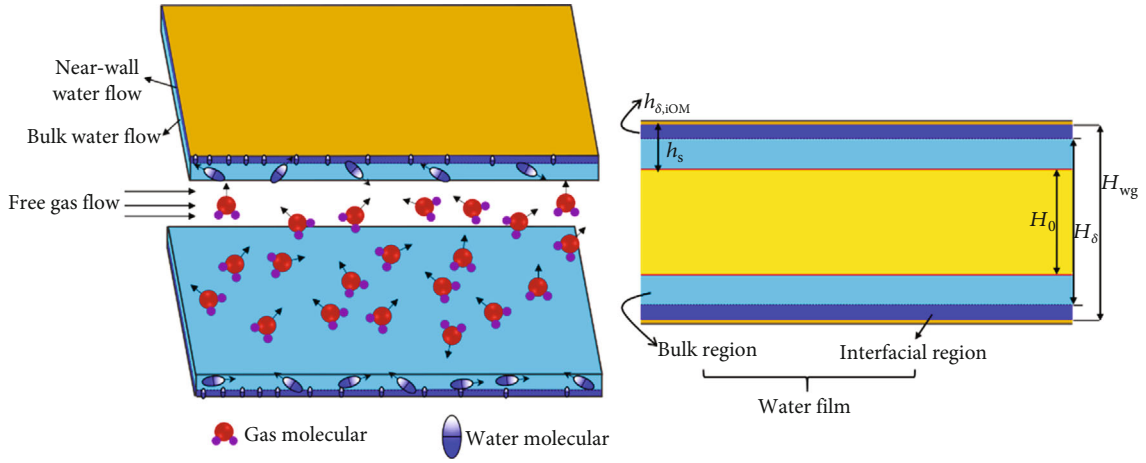

Figure 2: Illustration of the gas-water flow in nanoscale inorganic pores (viscous and slip flow of free gas in the pore center and the viscous flow of near-wall water and bulk water).

$\Pi(h_c)$ is the sum of the London-van der Waals force, the electrical force, and the structural force (negative for the hydrophobic surface [34]), given by

$$\Pi(h_c) = \frac{A_H}{h_c^3} + \frac{\varepsilon\varepsilon_0}{8\pi}\frac{(\varsigma_1 - \varsigma_2)^2}{h_c^2} + ke^{-h_c/\Gamma}. \tag{4}$$

The water saturation and water film thickness in a nanocapillary satisfy the following relationship

$$S_{wc} = 1 - \left(1 - \frac{h_c}{r_0}\right)^2. \tag{5}$$

Consequently, the effective flow radius r_{wg} and Knudsen number considering the water film for free gas are written as

$$r_{wg} = r_0\sqrt{1 - S_{wc}}, \tag{6}$$

$$K_{nc} = \frac{\lambda}{2r_{wg}}, \tag{7}$$

where λ is the MFP for a real gas, defined as [39]

$$\lambda = \frac{\mu_g}{P_p}\sqrt{\frac{\pi ZRT}{2M}}. \tag{8}$$

To represent the difference between ideal gas and real gas, the compressibility factor Z is considered and incorporated into the Equation (8). In this work, we use van der Waals' two-parameter principle of corresponding states to calculate compressibility factor, i.e., Z, as a function of pressure and temperature for any gas expressed by reduced temperature (T_r) and pressure (P_r). The gas compressibility factor (Z) can be expressed as [39]

$$\begin{aligned} Z &= \left(0.702e^{-2.5T_r}\right)P_r^2 - \left(5.524e^{-2.5T_r}\right)P_r + \left(0.044T_r^2 - 0.164T_r + 1.15\right), \\ P_r &= \frac{P_p}{P_c}, \\ T_r &= \frac{T}{T_c}. \end{aligned} \tag{9}$$

Moreover, Jarrahian and Heidaryan [46] developed a reliable and superior correlation to estimate the dynamic viscosity for real gas.

$$\mu_g = \mu_{g0}\left[1 + \frac{A_1}{T_r^5}\left(\frac{P_r^4}{T_r^{20} + P_r^4}\right) + A_2\left(\frac{P_r}{T_r}\right)^2 + A_3\left(\frac{P_r}{T_r}\right)\right]. \tag{10}$$

It should be noticed that the pore-confinement effect, which might lead to the critical property shift in nanopores, is not considered in this work due to its poor understanding.

As previously discussed, the N-S equations can be used to describe the fluid flow in nanopores. In the unidirectional pressure-driven nanopore flow, the governing equation for each region can be expressed as

$$\frac{dP}{dx} = -\frac{\mu_g}{r}\frac{d}{dr}\left(r\frac{dv_g}{dr}\right), r \in \left[0, r_{wg}\right], \tag{11a}$$

$$\frac{dP}{dx} = -\frac{\mu_{wb}}{r}\frac{d}{dr}\left(r\frac{dv_{wb}}{dr}\right), r \in \left[r_{wg}, r_\delta\right], \tag{11b}$$

$$\frac{dP}{dx} = -\frac{\mu_{wf}}{r}\frac{d}{dr}\left(r\frac{dv_{wf}}{dr}\right), r \in \left[r_\delta, r_0\right]. \tag{11c}$$

Based on Equation (11), the velocity profile for each region is given as

$$v_g = -\frac{r^2}{4\mu_g}\frac{dP}{dx} + c_g, r \in \left[0, r_{wg}\right], \tag{12a}$$

$$v_{wb} = -\frac{r^2}{4\mu_{wb}}\frac{dP}{dx} + c_{wb}, r \in \left[r_{wg}, r_\delta\right], \tag{12b}$$

$$v_{wf} = -\frac{r^2}{4\mu_{wf}}\frac{dP}{dx} + c_{wf}, r \in \left[r_\delta, r_0\right]. \tag{12c}$$

The multiple transport mechanisms of the viscous, slip, transition flow regimes (i.e., $0.0002 < K_n < 6$) are involved in gas-shale reservoirs. Therefore, a modified second-order slip boundary condition is applied to simulate the gas flow behavior. Moreover, the near-wall water can slip along the pore wall due to depletion force exerted by the hydrophobic surface. As such, boundary conditions of each region guarantying the continuity of velocity and mass conservation are expressed as follows:

$$\begin{aligned}
&\left.\frac{\partial v_g}{\partial r}\right|_{r=0} = 0,\\
&v_g\big|_{r=r_{wg}} = v_{wb}\big|_{r=r_{wg}} + v_{slip}\big|_{r=r_{wg}},\\
&v_{wb}\big|_{r=r_\delta} = v_{wf}\big|_{r=r_\delta},\\
&\mu_{wb}\left.\frac{\partial v_{wb}}{\partial r}\right|_{r=r_\delta} = \mu_{wf}\left.\frac{\partial v_{wf}}{\partial r}\right|_{r=r_\delta},\\
&v_{wf}\big|_{r=r_0} = -l_s\left.\frac{\partial v_{wf}}{\partial r}\right|_{r=r_0},
\end{aligned} \tag{13}$$

where l_s is the water slip length, which used to capture the water slip, described as [35]

$$l_s = \frac{C}{(1+\cos\theta)^2}. \tag{14}$$

It was confirmed by many scholars [35] that $C = 0.41$ fitted by the MD simulation data should be adopted.

Combining Equation (12) with boundary conditions in Equation (13), velocity profile for free gas is yield

$$\begin{aligned}
v_g = {} & \frac{r_{wg}^2 - r^2}{4\mu_g}\frac{dP}{dx} + \frac{A_1\lambda r_{wg} + A_2\lambda^2}{2\mu_g}\frac{dP}{dx} + \frac{r_\delta^2 - r_{wg}^2}{4\mu_{wb}}\frac{dP}{dx}\\
& + \frac{r_0^2 - r_\delta^2}{4\mu_{wf}}\frac{dP}{dx} + \frac{l_s r_0}{2\mu_{wf}}\frac{dP}{dx}, r \in \left[0, r_{wg}\right].
\end{aligned} \tag{15}$$

Consequently, the gas volume flux q_g is obtained by integration with respect to the radius

$$\begin{aligned}
q_g = {} & 2\pi\int_0^{r_{wg}} v_g r dr = \frac{\pi r_{wg}^4}{8\mu_g}\left(1 + 8C_1K_{nc} + 16C_2K_{nc}^2\right)\frac{dP}{dx}\\
& + \frac{\pi r_{wg}^2\left(r_\delta^2 - r_{wg}^2\right)}{4\mu_{wb}}\frac{dP}{dx} + \frac{\pi r_{wg}^2\left(r_0^2 - r_\delta^2\right)}{4\mu_{wf}}\frac{dP}{dx}\\
& + \frac{\pi r_{wg}^2 l_s r_0}{2\mu_{wf}}\frac{dP}{dx}.
\end{aligned} \tag{16}$$

In order to get the gas volumetric flux of nanoporous OM, a correction factor ξ, related to two essential structural parameters (i.e., tortuosity and porosity), is introduced [47]. Thus, the total gas volume flux through the OM can be calculated by

$$\begin{aligned}
Q_g = \xi\Bigg[& \frac{\pi r_{wg}^4}{8\mu_g}\left(1 + 8C_1K_{nc} + 16C_2K_{nc}^2\right)\frac{dP}{dx}\\
& + \frac{\pi r_{wg}^2\left(r_\delta^2 - r_{wg}^2\right)}{4\mu_{wb}}\frac{dP}{dx} + \frac{\pi r_{wg}^2\left(r_0^2 - r_\delta^2\right)}{4\mu_{wf}}\frac{dP}{dx}\\
& + \frac{\pi r_{wg}^2 l_s r_0}{2\mu_{wf}}\frac{dP}{dx}\Bigg].
\end{aligned} \tag{17}$$

The basic form of correction factor ξ is

$$\xi = \frac{\phi_{OM}}{\tau}. \tag{18}$$

According to the general Darcy's law [48], the AGP of OM can be characterized as

$$\begin{aligned}
k_{OM} = \frac{\phi_{OM}}{\tau}\Bigg[& \underbrace{\frac{\pi r_{wg}^4}{8A_{OM}}\left(1 + 8C_1K_{nc} + 16C_2K_{nc}^2\right)}_{\text{gas slippage}} + \underbrace{\frac{\mu_g}{\mu_{wb}}\frac{\pi r_{wg}^2\left(r_\delta^2 - r_{wg}^2\right)}{4A_{OM}}}_{\text{bulk water flow}}\\
& + \underbrace{\frac{\mu_g}{\mu_{wf}}\frac{\pi r_{wg}^2\left(r_0^2 - r_\delta^2\right)}{4A_{OM}}}_{\text{near-wall water flow}} + \underbrace{\frac{\mu_g}{\mu_{wf}}\frac{\pi r_{wg}^2 l_s r_0}{2A_{OM}}}_{\text{near-wall water slip}}\Bigg].
\end{aligned} \tag{19}$$

Equation (19) is the final expression of AGP for OM. Several permeability models at different boundary conditions can be obtained based on Equation (19).

(a) The intrinsic permeability

$$k_{\mathrm{OM-int}} = \frac{\phi_{\mathrm{OM}}}{\tau}\frac{\pi {r_0}^4}{8A_{\mathrm{OM}}}. \tag{20}$$

(b) The AGP in dry conditions

$$k_{\mathrm{OM-dry}} = \frac{\phi_{\mathrm{OM}}}{\tau}\frac{\pi {r_0}^4}{8A_{\mathrm{OM}}}\left(1 + 8C_1K_{\mathrm{nc}} + 16C_2{K_{\mathrm{nc}}}^2\right), \tag{21a}$$

$$K_{\mathrm{nc}} = \frac{\lambda}{2r_0}. \tag{21b}$$

(c) The AGP considering an immobile water film

$$k_{\mathrm{OM-immobile}} = \frac{\phi_{\mathrm{OM}}}{\tau}\frac{\pi {r_{\mathrm{wg}}}^4}{8A_{\mathrm{OM}}}\left(1 + 8C_1K_{\mathrm{nc}} + 16C_2{K_{\mathrm{nc}}}^2\right), \tag{22a}$$

$$K_{\mathrm{nc}} = \frac{\lambda}{2r_{\mathrm{wg}}}. \tag{22b}$$

2.2. Gas Flow Behavior through Hydrophilic Nanopores (iOM). Different from OM, the iOM consists of abundant minerals (e.g., quartz, clays, and pyrite), which has a strong affinity to water molecules. Therefore, it is reasonable to assume that when the gas and water coexist in inorganic pore simultaneously, a gas core surrounded by a water film occupies the pore center (Figure 2).

The water film thickness h_s inside a nanoslit is calculated by [33]

$$\Pi_s(h_s) = -\frac{RT}{V_{\mathrm{m}}}\ln\frac{P_v}{P^*}. \tag{23}$$

Here, $\Pi_s(h_s)$ is the disjoining pressure, described as [32]

$$\Pi_s(h_s) = \Pi_1(h_s) + \Pi_2(h_s) + \Pi_3(h_s), \tag{24}$$

where $\Pi_1(h_s)$ is the interaction between water film and a solid surface on the same side, $\Pi_2(h_s)$ is the interaction between water film and a solid surface at the opposite side, and $\Pi_3(h_s)$ is the interaction between two adsorbed films. Each component can be expressed as follows:

$$\Pi_1(h_s) = \frac{A_H}{h_s^3} + \frac{\varepsilon\varepsilon_0}{8\pi}\frac{(\varsigma_1-\varsigma_2)^2}{h_s^2} + k^* e^{-h_s/\Gamma}, \tag{25a}$$

$$\Pi_2(h_s) = \frac{A_H}{(H_0-h_s)^3} + \frac{\varepsilon\varepsilon_0}{8\pi}\frac{(\varsigma_1-\varsigma_2)^2}{(H_0-h_s)^2} + k^* e^{-(H_0-h_s)/\Gamma}, \tag{25b}$$

$$\Pi_3(h_s) = \frac{A_{H^*}}{(H_0-2h_s)^3}. \tag{25c}$$

The water saturation and water film thickness in a nanoslit satisfy the relationship

$$S_{\mathrm{ws}} = \frac{2h_s}{H_0}. \tag{26}$$

Consequently, the effective aperture and Knudsen number considering water film for free gas flow are characterized as

$$H_{\mathrm{wg}} = H_0(1 - S_{\mathrm{ws}}), \tag{27}$$

$$K_{\mathrm{ns}} = \frac{\lambda}{H_{\mathrm{wg}}}. \tag{28}$$

The governing equation for the pressure-driven flow through a slit pore in different regions is presented by

$$\frac{\partial^2 v_g}{\partial y^2} = -\frac{1}{\mu_{\mathrm{g}}}\frac{dP}{dx}, y \in \left[0, \frac{H_{\mathrm{wg}}}{2}\right], \tag{29a}$$

$$\frac{\partial^2 v_{\mathrm{wb}}}{\partial y^2} = -\frac{1}{\mu_{\mathrm{wb}}}\frac{dP}{dx}, y \in \left[\frac{H_{\mathrm{wg}}}{2}, \frac{H_\delta}{2}\right], \tag{29b}$$

$$\frac{\partial^2 v_{\mathrm{wf}}}{\partial y^2} = -\frac{1}{\mu_{\mathrm{wf}}}\frac{dP}{dx}, y \in \left[\frac{H_\delta}{2}, \frac{H_0}{2}\right]. \tag{29c}$$

Based on Equation (29), the velocity profile for each region yields to

$$v_g = -\frac{y^2}{2\mu_{\mathrm{g}}}\frac{dP}{dx} + c_g, y \in \left[0, \frac{H_{\mathrm{wg}}}{2}\right], \tag{30a}$$

$$v_{\mathrm{wb}} = -\frac{y^2}{2\mu_{\mathrm{wb}}}\frac{dP}{dx} + c_{\mathrm{wb}}, y \in \left[\frac{H_{\mathrm{wg}}}{2}, \frac{H_\delta}{2}\right], \tag{30b}$$

$$v_{\mathrm{wf}} = -\frac{y^2}{2\mu_{\mathrm{wf}}}\frac{dP}{dx} + c_{\mathrm{wf}}, y \in \left[\frac{H_\delta}{2}, \frac{H_0}{2}\right]. \tag{30c}$$

Compared with hydrophobic pores, the water slip velocity and slip length are negligible due to the strong attractive force induced by hydrophilic pore surface [35]. So, the boundary conditions of each region are given as

$$\begin{aligned}
&\left.\frac{\partial v_g}{\partial y}\right|_{y=0} = 0,\\
&v_g\big|_{y=\frac{H_{wg}}{2}} = v_{wb}\big|_{y=\frac{H_{wg}}{2}} + v_{slip}\big|_{y=\frac{H_{wg}}{2}},\\
&v_{wb}\big|_{y=\frac{H_\delta}{2}} = v_{wf}\big|_{y=\frac{H_\delta}{2}},\\
&\mu_{wb}\left.\frac{\partial v_{wb}}{\partial y}\right|_{y=\frac{H_\delta}{2}} = \mu_{wf}\left.\frac{\partial v_{wf}}{\partial y}\right|_{y=\frac{H_\delta}{2}},\\
&v_{wf}\big|_{y=\frac{H_0}{2}} = 0.
\end{aligned} \tag{31}$$

Combining with Eqs. (30) and (31), the gas velocity is expressed as

$$\begin{aligned}
v_g = {} & \frac{{H_{wg}}^2 - 4y^2}{8\mu_g}\frac{dP}{dx} + \frac{C_3\lambda H_{wg} + 2C_4\lambda^2}{2\mu_g}\frac{dP}{dx}\\
& + \frac{{H_\delta}^2 - {H_{wg}}^2}{8\mu_{wb}}\frac{dP}{dx} + \frac{{H_0}^2 - {H_\delta}^2}{8\mu_{wf}}\frac{dP}{dx}, y \in \left[0, \frac{H_{wg}}{2}\right].
\end{aligned} \tag{32}$$

The gas volume flux of a nanoslit can be further calculated through the integration of Equation (32) along the y -axis

$$\begin{aligned}
q_g = {} & 2\int_0^{H_{wg}/2} v_g W dy = \frac{W{H_{wg}}^3}{12\mu_g}\left(1 + 6C_3K_{ns} + 12C_4{K_{ns}}^2\right)\frac{dP}{dx}\\
& + \frac{WH_{wg}\left({H_\delta}^2 - {H_{wg}}^2\right)}{8\mu_{wb}}\frac{dP}{dx} + \frac{WH_{wg}\left({H_0}^2 - {H_\delta}^2\right)}{8\mu_{wf}}\frac{dP}{dx}.
\end{aligned} \tag{33}$$

Assuming the inorganic pores are composed by numerous paralleled nanoslits, the total gas volume flux of the iOM can be obtained by introducing a correction factor ς

$$\begin{aligned}
Q_g = {} & \varsigma\left[\frac{W{H_{wg}}^3}{12\mu_g}\left(1 + 6C_3K_{ns} + 12C_4{K_{ns}}^2\right)\right.\\
& \left. + \frac{WH_{wg}\left({H_\delta}^2 - {H_{wg}}^2\right)}{8\mu_{wb}} + \frac{WH_{wg}\left({H_0}^2 - {H_\delta}^2\right)}{8\mu_{wf}}\right]\frac{dP}{dx}.
\end{aligned} \tag{34}$$

The correction factor ς is defined as

$$\varsigma = \frac{\phi_{iOM}}{\tau}. \tag{35}$$

Consequently, the AGP of iOM can be calculated by

$$\begin{aligned}
k_{iOM} = {} & \frac{\phi_{iOM}}{\tau}\left[\frac{W{H_{wg}}^3}{12A_{iOM}}\left(1 + 6C_3K_{ns} + 12C_4{K_{ns}}^2\right)\right.\\
& \left. + \frac{\mu_g}{\mu_{wb}}\frac{WH_{wg}\left({H_\delta}^2 - {H_{wg}}^2\right)}{8A_{iOM}} + \frac{\mu_g}{\mu_{wf}}\frac{WH_{wg}\left({H_0}^2 - {H_\delta}^2\right)}{8A_{iOM}}\right].
\end{aligned} \tag{36}$$

Considering the impact of pore geometry, a shape factor $A(\zeta)$ is incorporated into the Equation (36) to obtain the final expression of AGP for iOM

$$\begin{aligned}
k_{iOM} = {} & \frac{\phi_{iOM}}{\tau}A(\zeta)\left[\underbrace{\frac{W{H_{wg}}^3}{12A_{iOM}}\left(1 + 6C_3K_n + 12C_4{K_n}^2\right)}_{\text{gas slippage}}\right.\\
& \left. + \underbrace{\frac{\mu_g}{\mu_{wb}}\frac{WH_{wg}\left({H_\delta}^2 - {H_{wg}}^2\right)}{8A_{iOM}}}_{\text{bulk water flow}} + \underbrace{\frac{\mu_g}{\mu_{wf}}\frac{WH_{wg}\left({H_0}^2 - {H_\delta}^2\right)}{8A_{iOM}}}_{\text{near-wall water flow}}\right],
\end{aligned} \tag{37}$$

where the aspect ratio ζ and shape factor $A(\zeta)$ are defined as [49]

$$\zeta = \frac{W}{H_0}, \tag{38a}$$

$$A(\zeta) = 1 - \frac{192}{\zeta\pi^5}\sum_{i=1,3,5,\cdots}^{\infty}\frac{\tanh\left(I\pi\zeta/2\right)}{i^5}. \tag{38b}$$

Equation (37) incorporates the effects of gas slippage and water film mobility on the gas flow. Based on Equation (37), several permeability models at different boundary conditions can be obtained as follows:

(a) Intrinsic permeability

$$k_{iOM-int} = \frac{\phi_{iOM}}{\tau}A(\zeta)\frac{W{H_0}^3}{12A_{iOM}}. \tag{39}$$

(b) The AGP in dry conditions

$$k_{iOM-dry} = \frac{\phi_{iOM}}{\tau}A(\zeta)\frac{W{H_0}^3}{12A_{iOM}}\left(1 + 6C_3K_{ns} + 12C_4{K_{ns}}^2\right), \tag{40a}$$

$$K_{ns} = \frac{\lambda}{H_0}. \tag{40b}$$

(c) The AGP considering an immobile water film

Table 1: Parameters used in the proposed models for validation.

Parameters	Value
The pore radius for OM, r_0 (nm)	50 [8]
The pore aperture for iOM, H_0 (nm)	100 [29]
The pore height for iOM, W (nm)	300
Porosity for OM, φ_{OM}	0.134
Porosity for iOM, φ_{iOM}	0.105
Tortuosity, τ	1.15
The contact angle of organic pore, θ_{OM} (°)	140 [35]
The contact angle of inorganic pore, θ_{iOM} (°)	30 [35]
The water viscosity within the bulk region, μ_{wb} (Pa·s)	8.9×10^{-4} [51]
The thickness of the interfacial region in organic pore, $h_{\delta,\mathrm{OM}}$ (nm)	0.5 [36]
The thickness of the interfacial region in inorganic pore, $h_{\delta,\mathrm{iOM}}$ (nm)	0.8 [36]
Temperature, T (K)	323
Pore pressure, P_p (MPa)	0.2 ~ 20
Critical temperature, T_c (K)	190.56 [39]
Critical pressure, P_c (MPa)	4.599
Ideal gas viscosity, μ_{g0} (Pa·s)	2.2×10^{-5}
Molecular weight, M (kg/mol)	0.016
Universal gas constant, R (J/(mol·K))	8.314
The relative humidity, RH (dimensionless)	0.8
The first-order slip coefficient in the organic pore, C_1	1.25 [8]
The second-order slip coefficient in the organic pore, C_2	0.23
The first-order slip coefficient in the inorganic pore, C_3	1.59
The second-order slip coefficient in the inorganic pore, C_4	0.47
The Hamaker constant for solid-gas-water interactions, A_H (J)	1×10^{-20} [33]
The Hamaker constant for water-gas-water interactions, A_{H^*} (J)	1.5×10^{-21}
The relative permittivity of media, ε (dimensionless)	81.5
Vacuum permittivity, ε_0 (F/m)	8.85×10^{-12}
The coefficient for the strength of the structural force in OM, κ (N/m^2)	-2×10^7 [33]
The coefficient for the strength of the structural force in iOM, κ^* (N/m^2)	1×10^7
Molar volume of water, V_m (m^3/mol)	1.8×10^{-5}
Gas-water surface tension for organic pore, γ (mN/m)	72
Characteristic decay length, Γ (nm)	2 [32]
Potentials difference between solid-water interface and water-gas interface, $\varsigma_1 - \varsigma_2$ (mV)	50
Fitting constant, Y_1 (dimensionless)	7.9 [39]
Fitting constant, Y_2 (dimensionless)	-9.0×10^{-6}
Fitting constant, Y_3 (dimensionless)	0.28

$$k_{\mathrm{iOM-immobile}} = \frac{\phi_{\mathrm{iOM}}}{\tau} A(\zeta) \left[\frac{W {H_{\mathrm{wg}}}^3}{12 A_{\mathrm{iOM}}} \left(1 + 6C_3 K_{\mathrm{ns}} + 12 C_4 {K_{\mathrm{ns}}}^2\right) \right],$$
$$K_{\mathrm{ns}} = \frac{\lambda}{H_{\mathrm{wg}}}. \tag{41a}$$

2.3. Apparent Gas Permeability for Shale Matrix. It is widely accepted that the shale matrix generally comprises of two components (i.e., OM and iOM). Here, the TOC content (α), which represents the volume ratio of organic nanopores to the total pores, is a weighting coefficient for gas flow through organic pores and inorganic pores, respectively [50]. Consequently, the AGP of the shale matrix is determined as

$$k_{\mathrm{AGP}} = \alpha k_{\mathrm{OM}} + (1 - \alpha) k_{\mathrm{iOM}}, \tag{42}$$

where k_{OM} and k_{iOM} can be found in Eqs. (19) and (37).

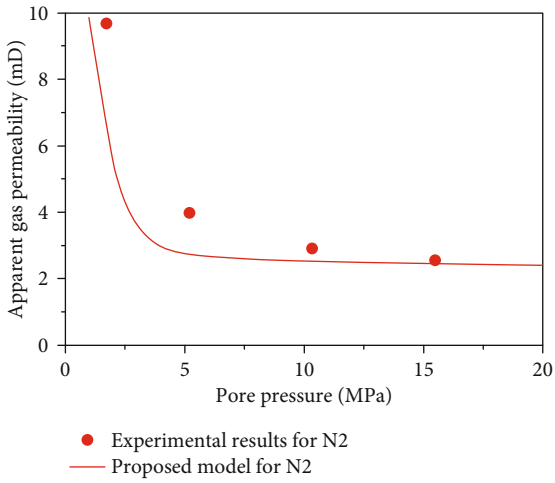

Figure 3: Validation of the proposed model for gas transport through organic pores.

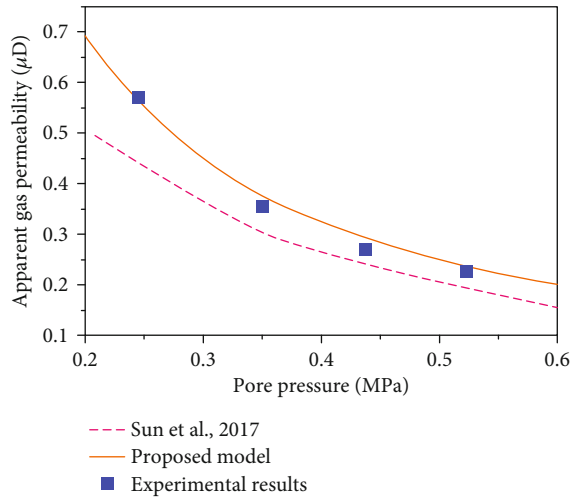

Figure 4: Validation of the proposed model for gas transport through inorganic pores.

3. Model Validation

The previous experimental data and analytical model results are applied to validate the unified gas-transport model for both organic and inorganic porous media. The parameters used for validation are shown in Table 1.

As we mentioned in the introduction, there are few indoor experiments and limited theories of the gas flow in moist hydrophobic-nanopores. Therefore, the published experimental data [8] at the dry condition is collected to verify our AGP model of OM at dry conditions firstly (Equation (21)). In detail, the mean pore size distribution of the shale sample is about 30 (nm), and the matrix permeability of Pierre shale was measured with nitrogen gas through the unsteady-state method. To remove the initial water, the shale sample was vacuumed and dried at 105°C. In this case, these data are appropriate to clarify the reliability of the proposed model for cylindrical organic pores in dry conditions. As shown in Figure 3, the proposed model fits well with the experimental data, and the gas permeability increases with decreasing pore pressure ascribed to the gas slippage.

For inorganic porous media, the model constructed in this paper is based on the assumption that the water film and gas can transport through nanoslit pores simultaneously. Because the difficulty of laboratory experiment for gas-water two-phase flow on shale samples, the published data of fluid flow behavior in nanochannels using laboratory-on-chip approach [29] are applied to validate our proposed model (Equation (37)). One type of gas-water distribution is that water is around the inner wall and gas occupies the central portion of the channel [29], which is consistent with our model assumption. Besides, the gas permeability model proposed by Sun et al. [52] is also used to compare with our model. As illustrated in Figure 4, our proposed model agrees better with the experimental data than Sun's model. This is because of the Sun's model based on the Beskok and Karniadakis [53] basic equation combining with the general second-order slip boundary considering a static water film. The mobility of water film is neglected in their model, which results in an underestimation of the gas conductance. In contrast, our model further considering the nanoconfined water film flow is more suitable to describe gas transport behavior under reservoir conditions.

Table 2: Numerical values of parameters used in the model's sensitivity analysis.

Parameters	Value
The pore radius for OM, r_0 (nm)	5-50 [36]
The pore aperture for iOM, H_0 (nm)	5-50
The pore height for iOM, W (nm)	5-350
The contact angle of organic pore, θ_{OM} (°)	90-160 [35]
The contact angle of inorganic pore, θ_{iOM} (°)	0-85 [35]
Pore pressure, P_p (MPa)	0.3-60
TOC contents, α	0-1.0 [47]

4. Sensitivity Analysis

The main novelty of this research is obtaining gas permeability for OM and iOM by further considering the impact of nanoconfined water film flow. Based on our model, the evolution of gas permeability at various boundary conditions is investigated firstly. Then, the gas flow capacity and the contributions of gas slippage and water film mobility under different pore dimensions, pressures, and surface wettability are discussed in detail. Finally, the impacts of pore structures (i.e., pore geometry and TOC contents) and a real gas effect on gas flow are extensively investigated. The input parameters used for calculation are listed in Table 2, except where otherwise stated.

4.1. The Gas Permeability Evolution at Three Boundary Conditions. The boundary conditions play a vital role in determining the behaviors of gas flow in nanopores. Currently, common conditions applied in simulations or

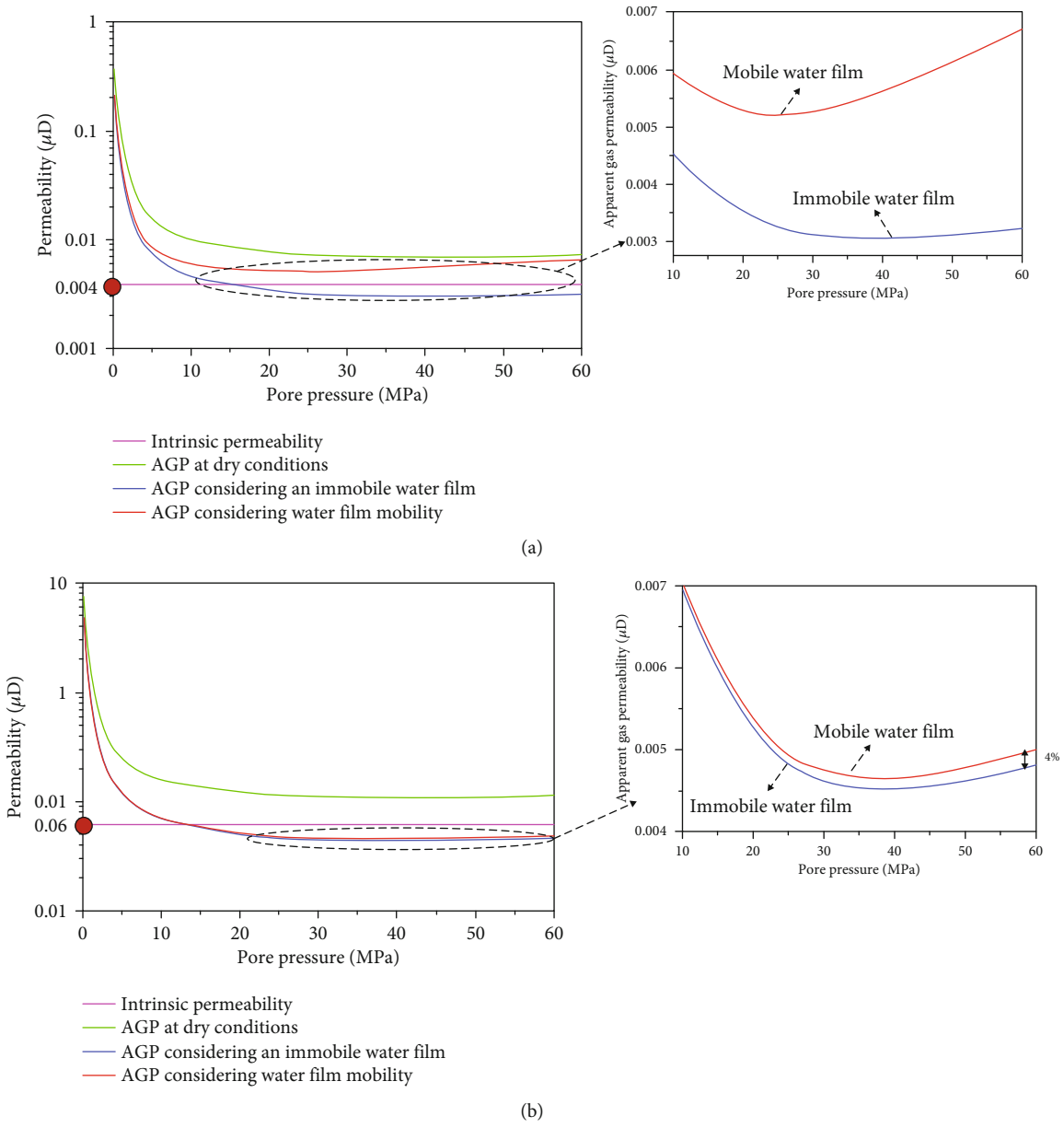

Figure 5: The gas permeability varies with pore pressure under different boundary conditions: (a) OM ($r_0 = 5$ nm, $\theta_{OM} = 145°$); (b) iOM ($H_0 = 10$ nm, $\zeta = 3$, $\theta_{iOM} = 30°$).

modeling work are dry conditions and moist conditions (i.e., an immobile water film and a mobile water film). There is still no consensus as to how the water affects gas flow in nanopores, and the mechanisms are not yet well understood. Therefore, a comprehensive analysis of the effects of water film on the gas flow is required, especially in nanopores with different surface wettability.

Obviously, the gas permeability increases with the decrease of pore pressure at three boundary conditions (i.e., dry condition, an immobile water film, and a mobile water film), while the intrinsic permeability keeps constant (Figure 5). As we all know, the intrinsic permeability is an inherent property of a porous media, which mainly depends on the pore structures (Eqs. (20) and (39)). In contrast, under other boundary conditions, the gas slippage improves flow capacity especially at low pressure ($P_p < 10$ (MPa)). Furthermore, the AGP reaches the maximum at dry conditions, followed by with a mobile water film and then with an immobile water film during depressurization (Figure 5). For dry conditions, gas conductance is improved by gas slippage due to free gas occupying the pore totally. However, under moist conditions, an immobile water film decreases the gas transport capacity by reducing the effective nanopore size, but the mobility of water film can partially offset its negative impact (Eqs. (19) and (37)). Compared with iOM, the enhancement of water film mobility to gas flow is obvious in OM because the near-wall water slipping increases a gas slip velocity at the boundary. Therefore, a mobile water film for gas flow in nanopores, especially for the organic-rich shale, needs to be considered at reservoir conditions.

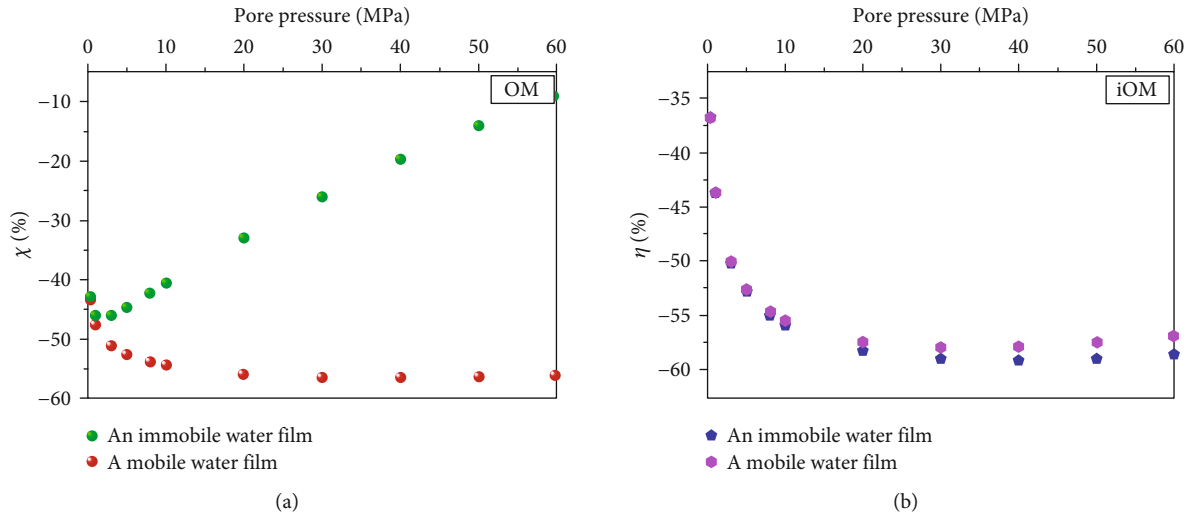

FIGURE 6: The differences of AGP at dry conditions and moist conditions (i.e., an immobile water film and a mobile water film): (a) OM ($r_0 = 5$ nm, $\theta_{OM} = 145°$); (b) iOM ($H_0 = 10$ nm, $\theta_{iOM} = 30°$).

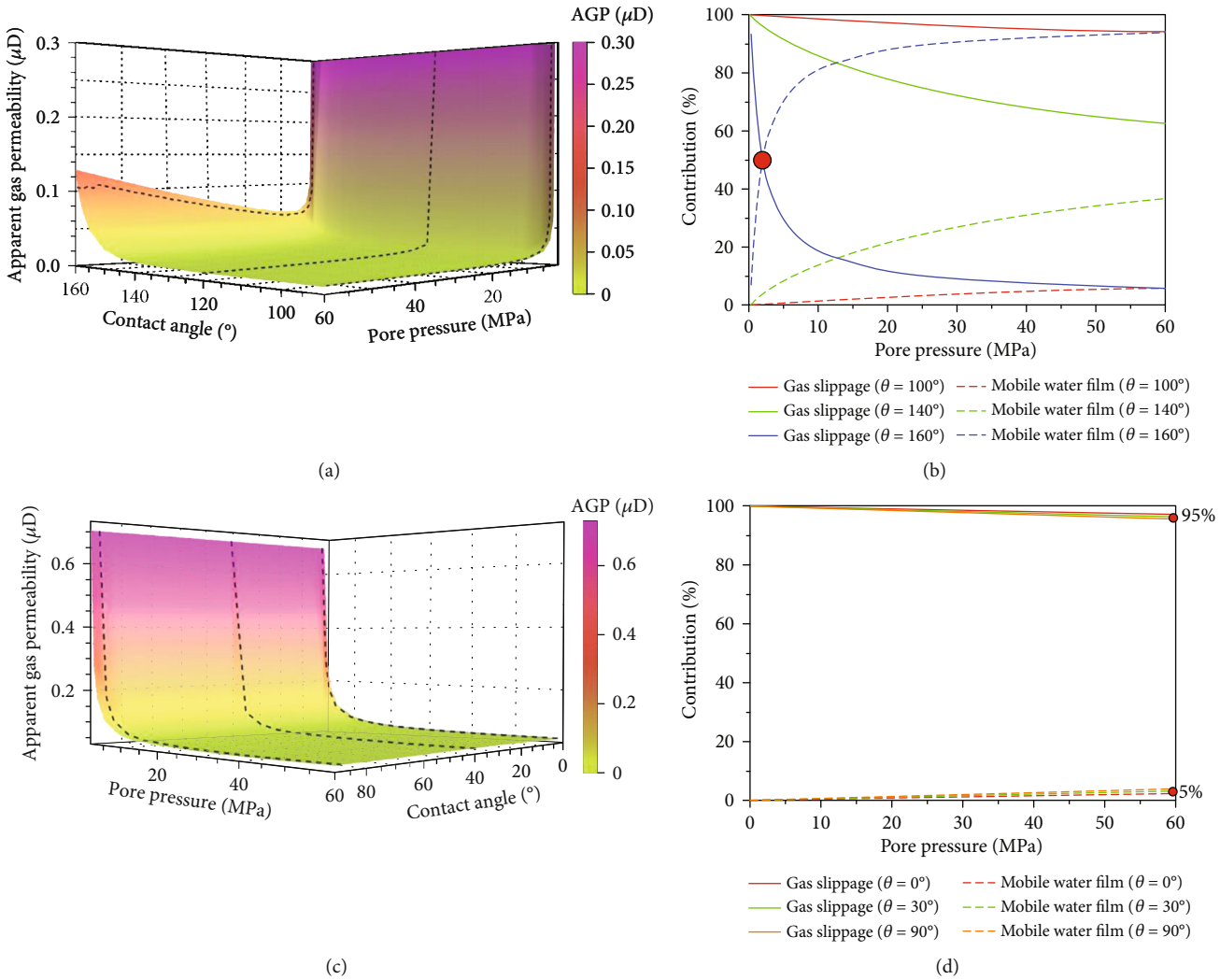

FIGURE 7: The impacts of pore pressure and contact angle on the gas flow. (a) The AGP of OM varies with pore pressure at different contact angles. (b) Contributions of gas slippage and water film mobility to gas flow in OM. (c) The AGP of iOM varies with pore pressure at different contact angles. (d) Contributions of gas slippage and water film mobility to gas flow in iOM.

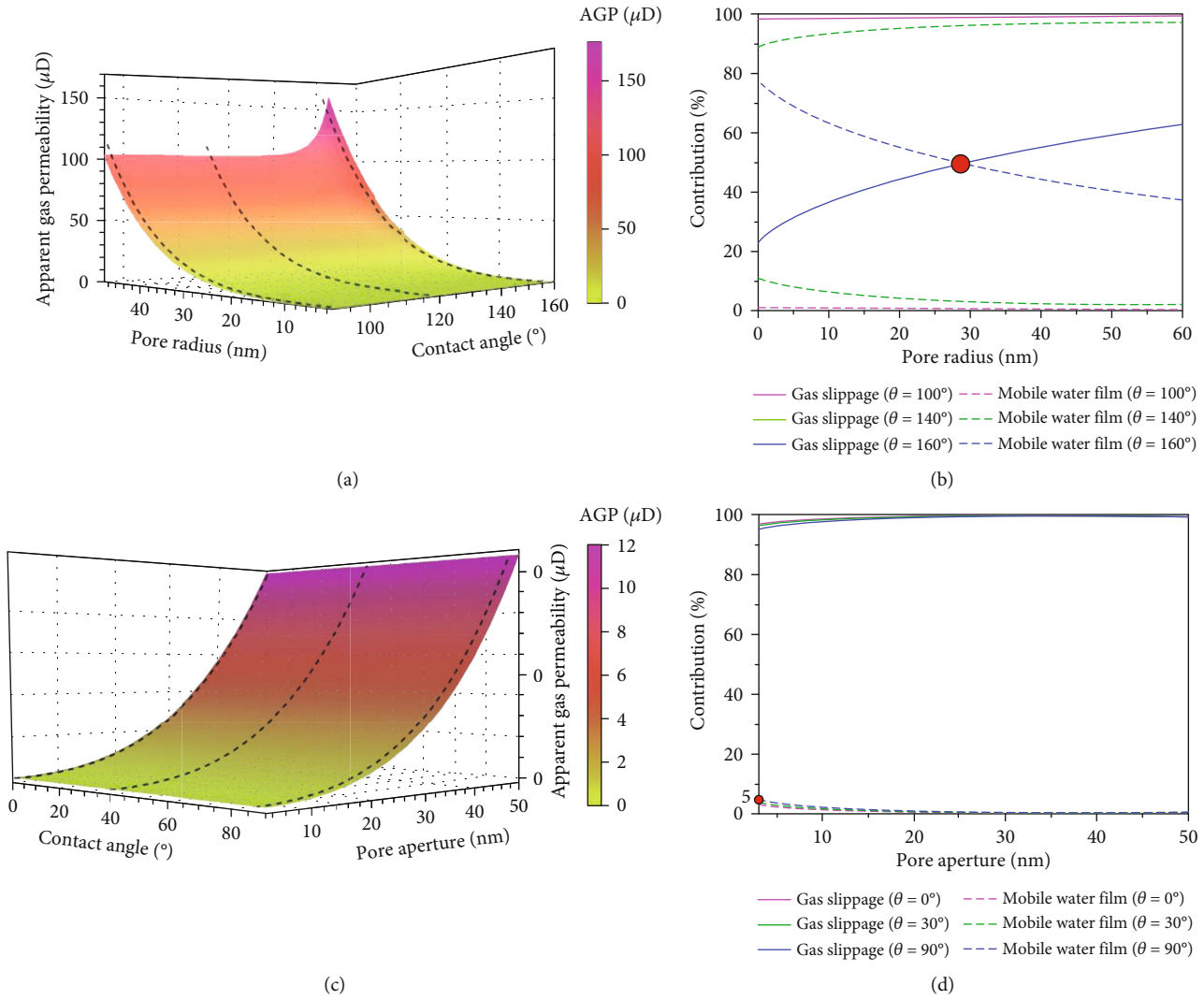

Figure 8: The impacts of pore size and contact angle on gas flow. (a) The AGP of OM varies with pore radius at different contact angles. (b) Contributions of gas slippage and water film mobility to gas flow in OM. (c) The AGP of iOM varies with pore apertures at different contact angles. (d) Contributions of gas slippage and water film mobility to gas flow in iOM.

To further analyze the impact of water film on gas flow, two parameters χ and η for OM and iOM, representing the relative difference of AGP between dry and moist conditions, are introduced

$$\chi = \frac{\left(k_{\mathrm{I}} - k_{\mathrm{OM-dry}}\right)}{k_{\mathrm{OM-dry}}} \times 100\%, \tag{43a}$$

$$\eta = \frac{\left(k_{\mathrm{II}} - k_{\mathrm{iOM-dry}}\right)}{k_{\mathrm{iOM-dry}}} \times 100\%, \tag{43b}$$

where the subscripts I and II represent two cases in moist conditions (i.e., an immobile water film and a mobile water film) for OM and iOM, respectively. k_{I} and k_{II} can be found in Eqs. (19), (22), (37), and (41).

Compared with that in dry conditions, the real gas flow decreases in moist conditions with mobile or nonmobile water film. This is because the presence of a water film occupies the pore volume by reducing the effective flow size for gas and therefore decreases the gas transport capacity. It is further noticed that the mobility of water film can compensate for its negative effect up to 50% by enhancing gas flow, which is remarkable in OM (Figure 6(a)). The reason is that, in contrast to static water molecules, a mobile water film can increase the gas slip velocity at the boundary to improve the gas conductance. Moreover, the near-wall water can slip fast along the hydrophobic surface, which leads to a higher gas velocity in organic pores than that in inorganic pores (Eqs. (19) and (37)). Noticed that the difference between considering and without considering water film mobility is more obvious at the higher-pressure range (30 (MPa)<P_p <60 (MPa)), which will be discussed in Section 4.3.

4.2. Effects of Pore Dimensions, Pressures, and Surface Wettability. As we mentioned before, gas flow in moist conditions is dominated by gas slippage and water film mobility. To achieve a better understanding of gas transport behavior

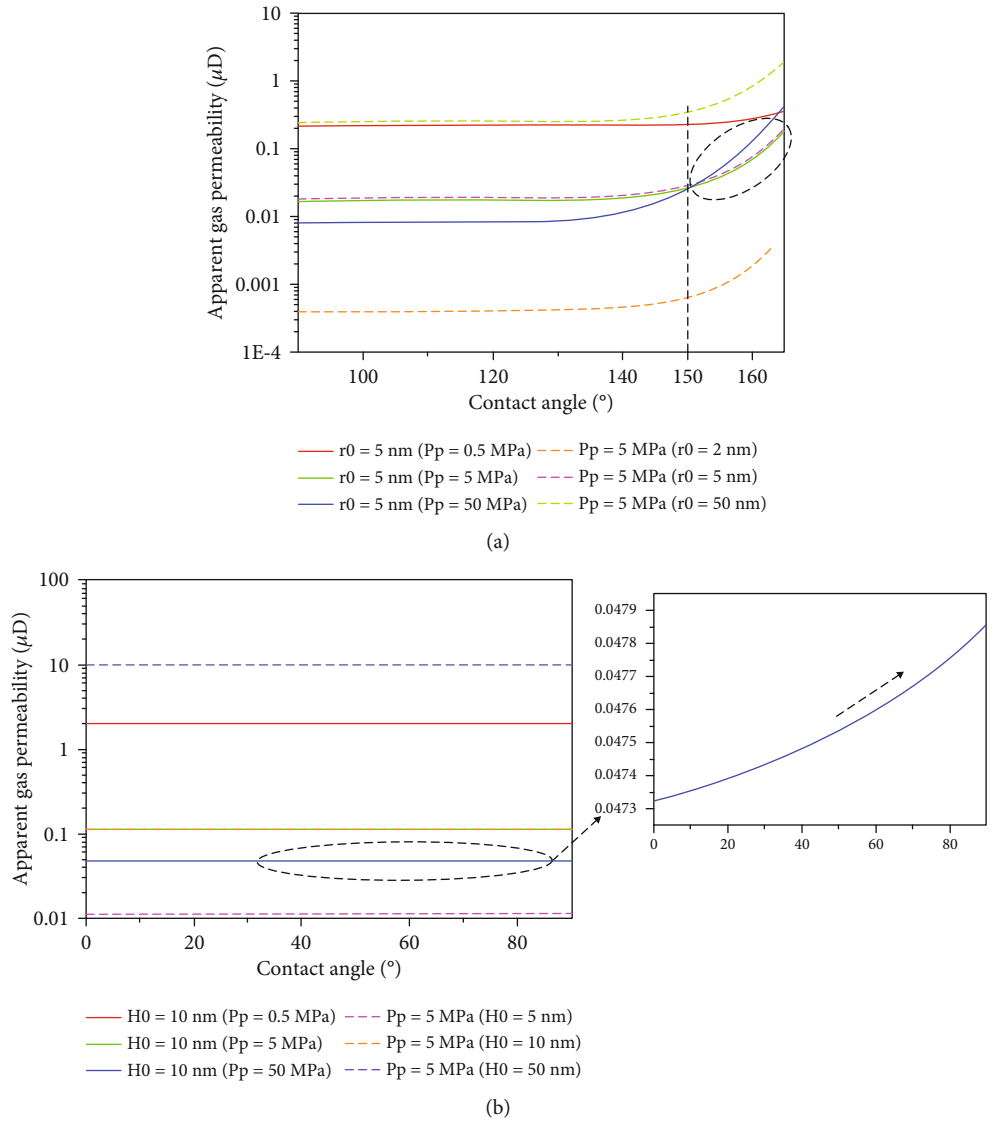

Figure 9: The coupled impacts of pore size, pore pressure, and contact angle on gas flow in (a) OM and (b) iOM.

through nanopores, it is significant to figure out concrete influence factors, including pore dimensions, pressures, and surface wettability (i.e., contact angle).

As shown in Figures 7(a) and 7(c), generally, the AGP increases by pore pressure decreasing, which is more significant at low pressure ascribed to the enhancement of gas slippage. Noted that when the contact angle is larger than 145°, the AGP of OM first decreases then increases during depressurization from 60 (MPa) to 0.3 (MPa) (Figure 7(a)). This is because the gas flow capacity is improved by water film mobility at the higher pressure range (40 (MPa)$<P_p<$60 (MPa)), while it is enhanced by gas slippage at the lower pressure range (0.3 (MPa)$< P_p <$10 (MPa)). Furthermore, the AGP of OM increases with contact angle (θ_{OM}) increasing from 90° to 160°, especially when the θ_{OM} is larger than 145° (Figure 7(a)). In contrast, the AGP of iOM is not sensitive to the contact angle (Figure 7(c)). Owing to the fact that a larger contact angle ($90° < \theta_{OM} < 180°$) corresponds to a relative lower viscosity and a larger slip length of near-wall water in the hydrophobic pore, which leads to a higher gas slip velocity at the boundary (Equation (15)). On the contrary, strong attractive force induced from a hydrophilic surface ($0° < \theta_{iOM} < 90°$) tends to result in an ordered arrangement of water molecules within several molecular diameters near the wall. An increase of water viscosity within the interfacial region limits its mobility further. Consequently, the water film without slip at the boundary (i.e., inorganic pores) has little impacts on the gas flow.

Moreover, the contributions of gas slippage and water film mobility to gas flow in OM and iOM under different pressures and contact angles are quantified (Figures 7(b) and 7(d)). When the contact angle is small (<145°), the contribution of gas slippage is always larger than that of water film mobility, whereas the result can possibly reverse in OM with the contact angle larger than 145° and pressure over than 5 (MPa) (Figure 7(b)). It further indicates that water slip in superhydrophobic nanopores is the main reason for gas flow enhancement. Moreover, the trend of the contributions

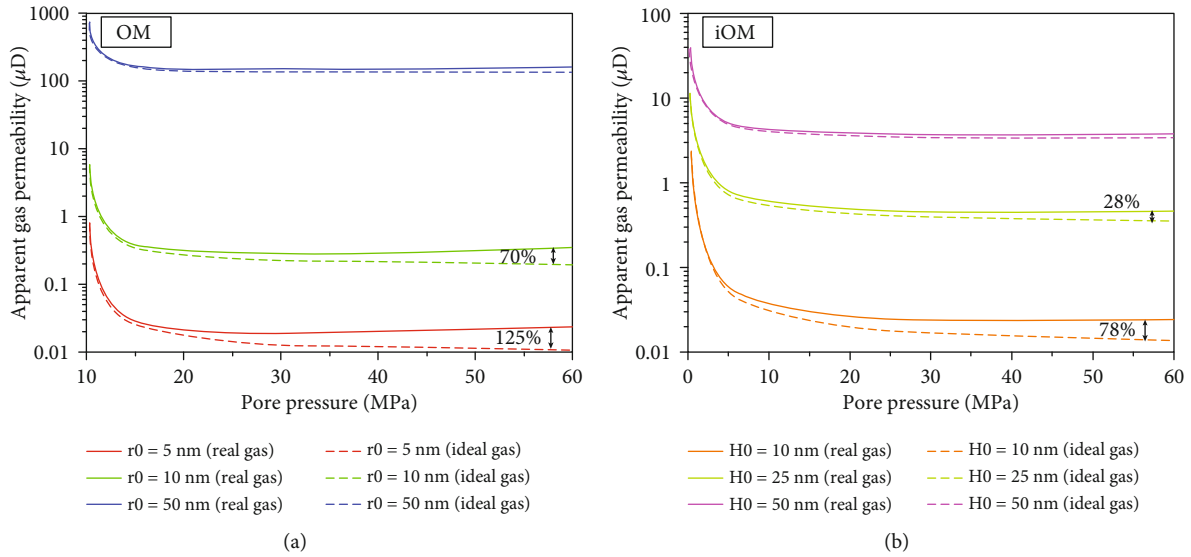

Figure 10: The AGP of (a) OM and (b) iOM varies with pore pressure for real gas and ideal gas at different pore dimensions.

of different effects varies with pressure for real gas flow. When depressurization occurs, the contribution of gas slippage increases gradually, but the contribution of water film mobility decreases. It is worth noting that the contribution of water film mobility to gas conductance in inorganic pores is no more than 5%; nonetheless, it still cannot be neglected for the low permeability shale (Figure 7(d)).

From Figures 8(a) and 8(c), the AGP positively correlated with pore size at a certain contact angle for both OM and iOM owing to the power-law relationship between gas conductance and pore radius/aperture based on Eqs. (19) and (37). Moreover, an increase of contact angle enhances gas transport capacity significantly in organic pores, whereas it has fewer impacts on gas flow in inorganic pores, which is consistent with the conclusion we obtained before.

Similar to gas slippage, the contribution of water film mobility to gas flow is larger in smaller pores at a certain contact angle (Figures 8(b) and 8(d)). Noticed that when the organic pore radius is smaller than 25 (nm) with a large contact angle (>160°), the contribution of water film mobility is larger than gas slippage (Figure 8(b)). It is interesting to investigate the underlying mechanisms behind the above phenomenon, which will be discussed in Section 4.3.

As shown in Figure 9, the AGP of OM increases with contact angle increasing especially when the θ_{iOM} is larger than 145°, which is attributed to a higher gas slip velocity at the boundary induced by a low-viscosity water slip along the pore surface (Figure 9(a)). Generally, the lower the pressure condition, the higher is the gas permeability. However, this conclusion is not applied to a large contact angle; for example, when the θ_{OM} is larger than 150°, the AGP of OM at 50 (MPa) is equal and even larger than that at 5 (MPa) (Figure 9(a)). The key mechanism lies in a real gas effect, which will be discussed in detail in Section 4.3.

4.3. The Real Gas Effect. As shown in Figure 10, the real gas effect improves gas conductance significantly in small pores

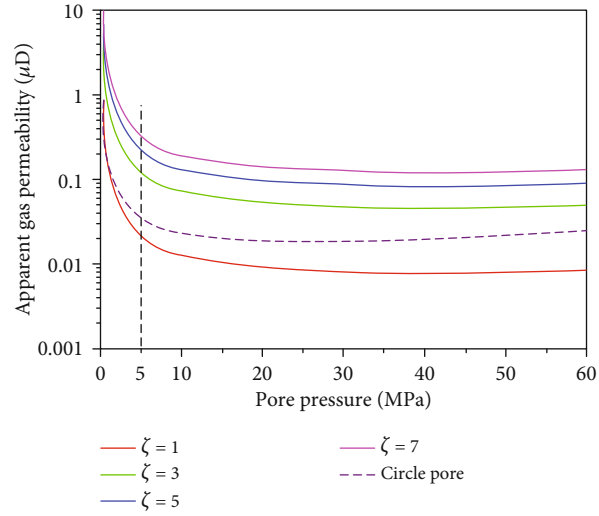

Figure 11: The impact of pore geometry on gas flow ($H_0 = 2r_0 = 10$ (nm)).

with high pressure. Moreover, compared with iOM, the real gas effect could greatly alter the AGP in the OM (i.e., up to 125%) for the pressure and pore radius of 60 (MPa) and 5 (nm), respectively (Figure 10(a)). Different from that in dry conditions, gas flow in moist conditions is dominated by gas slippage and water film mobility. The real gas viscosity can increase distinctly from 2.2×10^{-5} (Pa · s) to 7.5×10^{-5} (Pa · s) when the pore pressure increases from 0.5 (MPa) to 60.0 (MPa) at temperature of 323 (K). The gas viscosity increase can enhance the water film mobility and therefore improve gas flow capacity (Eqs. (19) and (37)). On the other hand, the real gas compressibility factor follows a nonmonotonic trend with pressure [42]. Both the increasing viscosity and compressibility factor variation will increase the MFP and K_n of gas molecules, which leads to the increment of

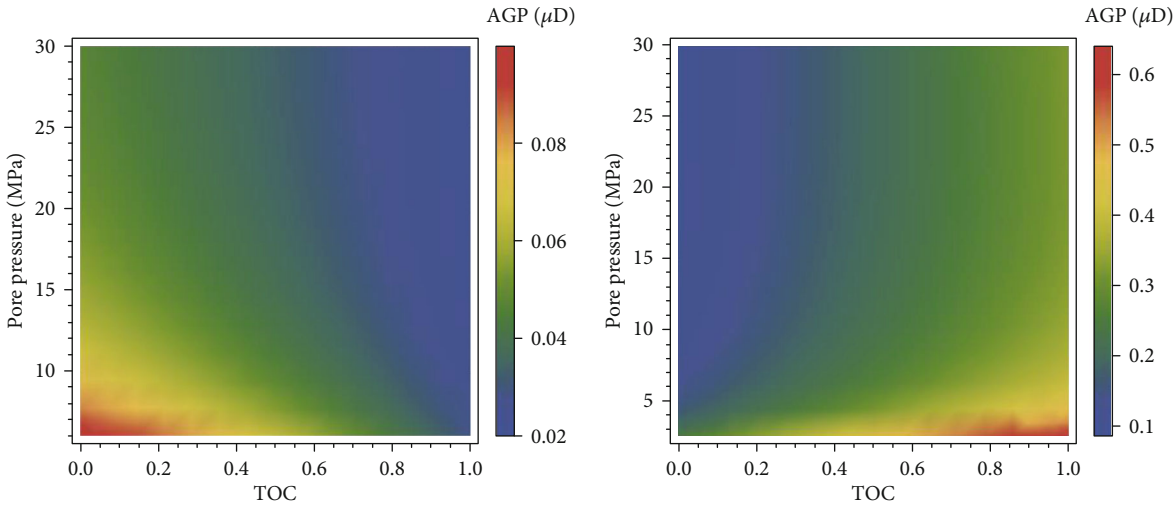

(a) $H_0 = 2r_0 = 10$ (nm) ($\zeta = 3$) (b) $H_0 = r_0 = 10$ (nm) ($\zeta = 5$)

Figure 12: The impact of TOC contents on the AGP of shale.

gas conductance. Therefore, it is necessary to consider the real gas effect at moist conditions.

4.4. Effects of the Pore Structures. Besides the multiple mechanisms, the pore structures of the matrix are also important to real gas flow. Here, we mainly discussed the impacts of pore geometry and TOC contents on the gas flow.

4.4.1. Aspect Ratio. Gas conductance in organic nanopores with a circular cross-section is stronger than that in inorganic pores with a rectangular cross-section when the aspect ratio (ζ) is smaller than 3, and vice versa when the ζ is larger than 3 (Figure 11). The reason is that the fluid flow area in a circular pore is larger than that in a slit pore when the two type pores at the same pore size. Besides, the water film mobility in organic pores enhances gas flow further. Moreover, gas transport capacity in inorganic pores with a rectangular cross-section increases with an aspect ratio increasing under a constant aperture. This is due to the larger the aspect ratio, the greater the surface area for gas flow, and the higher gas conductance. It is worth noting that gas flow can be dramatically improved with ζ from 1 to 3, while it is not sensitive to large ζ (>5). This is closely related to the variation law of pore geometry $A(\zeta)$ with aspect ratio ζ, which is discussed in the previous study [49]. Also, the impact of ζ on gas flow is evident when the pressure is less than 5 (MPa) from Figure 11, which results from the strong gas slippage induced by a large ζ. Therefore, we should pay more attention to the impact of pore geometry on fluid flow at the nanoscale as abundant nanopores with various pore cross-sections can be encountered in shale reservoir applications.

4.4.2. TOC Contents. The TOC contents of shale reservoirs are various in different basins [47]. Additionally, the enhancement of water film mobility to gas flow is more significant in OM. Thus, it is attractive to analyze the AGP evolution of shale with different TOC contents. Here, two cases of shale matrix with the TOC contents varying from 0 to 1 are presented in Figures 12(a) and 12(b) based on Equation (42). Results indicate that the TOC contents can enhance or reduce the AGP depending on the pore size difference between OM and iOM. The increase of TOC contents decreases the AGP of the shale matrix when the pore size is comparable between the two components (Figure 12(a)); however, opposite results can be obtained when the pore size of OM is larger than that of iOM (i.e., Figure 12(b), $H_0 = r_0 = 10$ (nm)). As we discussed before when the size of two types of pores is same and the aspect ratio is 3, the gas flow capacity through slit pores is greater than that in circular pores (Figure 11); thus, a larger TOC contents mean much more low conductive circular organic pores for gas flow. However, if the size of organic pores is little larger than the inorganic pores (i.e., $H_0 = r_0 = 10$ (nm)), plus the enhancement of water slip in organic pores, the gas conductance of OM is larger than iOM even though the inorganic pores have a large aspect ratio. Therefore, the TOC contents can possibly increase the AGP of the shale matrix.

5. Conclusions

A new model of the real gas transport in both organic and inorganic nanopores has been developed which takes into account, for the first time in literature, an important pore-level physics, i.e., the nanoconfined water film flow, in shales under reservoir conditions. The model was extensively used to analyze the contributions of gas slippage and water film mobility to gas flow at different nanopore dimensions, pressure, and surface wettability conditions. Several conclusions are drawn and listed below:

(1) Compared to the dry conditions, the gas flow capacity decreases under moist conditions whether the water film is mobile or not. If the water film is mobile, however, the film compensates its negative effect by increasing the gas flow up to 50% compared to the stagnant water film situations

(2) The AGP of OM/iOM decreases for smaller pore sizes. It increases by depressurization when the contact angle is smaller than 145°. When the contact angle is larger than 145°, the AGP of OM initially decreases and then increases during the depressurization process. Moreover, the AGP of OM increases for the larger contact angle values due to the water slip, whereas the AGP of iOM is not sensitive to the contact angle values

(3) Compared with iOM, gas transport capability in OM is greatly enhanced by the water film flow. Moreover, the contribution of water film flow is more pronounced in smaller pores with a large contact angle, especially at higher pressures

(4) The real-gas effect enhances gas flow by improving both gas slippage and water film mobility under moist conditions, which is more pronounced in smaller pores at higher pressures

(5) The TOC contents can vary the AGP of shale matrix depending on the pore size differences between the OM and iOM. Moreover, larger aspect ratios cause higher gas conductance of the iOM

Nomenclature

R: Universal gas constant (J/(mol·K))
M: Methane molar mass (kg/mol)
P_p: Pore pressure (MPa)
T: Temperature (K)
μ_{g0}: Viscosity for an ideal gas (Pa·s)
μ_g: Viscosity for real gas (Pa·s)
μ_{wb}: Viscosity for bulk water (Pa·s)
μ_{wf}: Viscosity for near-wall water (Pa·s)
λ: Mean free path for real gas (μm)
Z: Gas compressibility factor (dimensionless)
T_c: Critical temperature (K)
P_c: Critical pressure (MPa)
T_r: Reduced temperature (dimensionless)
P_r: Reduced pressure (dimensionless)
Y_1: Fitting constant (dimensionless)
Y_2: Fitting constant (dimensionless)
Y_3: Fitting constant (dimensionless)
r_0: The initial pore radius for OM (nm)
r_δ: The pore radius for OM considering near-wall water film (nm)
r_{wg}: The effective pore radius for gas flow in organic pores (nm)
H_0: The initial pore aperture for iOM (nm)
H_δ: The pore aperture for iOM considering near-wall water film (nm)
H_{wg}: The effective pore aperture for gas flow in inorganic pores (nm)
W: Pore width for inorganic pore (nm)
ζ: Aspect ratio
$A(\zeta)$: Pore geometry
θ_{OM}: Contact angle for organic pore (°)
θ_{iOM}: Contact angle for inorganic pore (°)
l_s: Slip length for near-wall water in organic pore (nm)
ϕ_{OM}: Porosity for OM
ϕ_{iOM}: Porosity for iOM
τ: Tortuosity
α: TOC contents (%)
ξ: Correction factor for OM (dimensionless)
ς: Correction factor for iOM (dimensionless)
h_c: Water film thickness in organic pore (nm)
h_s: Water film thickness in inorganic pore (nm)
$h_{\delta,\mathrm{OM}}$: The thickness of the interfacial region in organic pore (nm)
$h_{\delta,\mathrm{iOM}}$: The thickness of the interfacial region in inorganic pore (nm)
K_n: Knudsen number (dimensionless)
K_{nc}: The effective Knudsen number for gas flow in OM (dimensionless)
K_{ns}: The effective Knudsen number for gas flow in iOM (dimensionless)
S_{wc}: Water saturation in OM
S_{ws}: Water saturation in iOM
C_1: The first-order slippage coefficient for gas flow in organic pore (dimensionless)
C_2: The second-order slippage coefficient for gas flow in organic pore (dimensionless)
C_3: The first-order slippage coefficient for gas flow in inorganic pore (dimensionless)
C_4: The second-order slippage coefficient for gas flow in inorganic pore (dimensionless)
P_v: Water vapor pressure in the gaseous phase (MPa)
P_v/P^*: RH = Relative humidity (dimensionless)
A_H: The Hamaker constant for solid-gas-water interactions (J)
A_{H^*}: The Hamaker constant for water-gas-water interactions (J)
ε: The relative permittivity of media (dimensionless)
ε_0: Permittivity in vacuum (F/m)
κ: The coefficient for the strength of the structural force for OM (N/m^2)
κ^*: The coefficient for the strength of the structural force for iOM (N/m^2)
V_m: Molar volume of water (m^3/mol)
Γ: Characteristics decay length (nm)
$\varsigma_1 - \varsigma_2$: Potentials difference between solid–water interface and water–gas interface (mV)
$\Pi_c(h_c)$: Disjoining pressure between water film and solid surface for organic pores (MPa)
$\Pi(h_c)$: Total disjoining pressure for organic pores (MPa)
$\Pi_s(h_s)$: Disjoining pressure of water film inside inorganic pores (MPa)
$\Pi_1(h_s)$: Disjoining pressure of water film caused by inorganic surface at the same side (MPa)
$\Pi_2(h_s)$: Disjoining pressure of water film caused by inorganic pore surface at opposite side (MPa)
$\Pi_3(h_s)$: Disjoining pressure caused by two adsorbed water films in inorganic pore (MPa)
q_g: Gas volume flux in a single nanochannel (m^3)
Q_g: Total gas volume flux for a porous media (m^3)

k_{OM}: Apparent gas permeability for OM (μm^2)
k_{iOM}: Apparent gas permeability for iOM (μm^2)
k_{AGP}: Apparent gas permeability for shale matrix (μm^2).

Data Availability

The data used to support the findings of this study are included within the article.

Conflicts of Interest

The authors declare that they have no conflicts of interest.

Acknowledgments

The authors would like to acknowledge the financial supports of the National Natural Science Foundation for Youth (File No. 51804334) and the National Natural Science Foundation of China (U19B6003).

References

[1] H. Singh and F. Javadpour, "Langmuir slip-Langmuir sorption permeability model of shale," *Fuel*, vol. 164, pp. 28–37, 2016.

[2] Annual Energy Outlook, *With projections to 2040*, Government Printing Office, 2015.

[3] Y. Wu, L. Cheng, L. Ma et al., "A transient two-phase flow model for production prediction of tight gas wells with fracturing fluid-induced formation damage," *Journal of Petroleum Science and Engineering*, vol. 199, 2021.

[4] T. Zhang, X. Li, Z. Sun et al., "An analytical model for relative permeability in water-wet nanoporous media," *Chemical Engineering Science*, vol. 174, pp. 1–12, 2017.

[5] C. R. Clarkson, N. Solano, R. M. Bustin et al., "Pore structure characterization of North American shale gas reservoirs using USANS/SANS, gas adsorption, and mercury intrusion," *Fuel*, vol. 103, pp. 606–616, 2013.

[6] F. Javadpour, D. Fisher, and M. Unsworth, "Nanoscale gas flow in shale gas sediments," *Journal of Canadian Petroleum Technology*, vol. 46, no. 10, 2007.

[7] H. Singh, F. Javadpour, A. Ettehadtavakkol, and H. Darabi, "Nonempirical apparent permeability of shale," *SPE Reservoir Evaluation & Engineering*, vol. 17, no. 3, pp. 414–424, 2014.

[8] R. Nazari Moghaddam and M. Jamiolahmady, "Slip flow in porous media," *Fuel*, vol. 173, pp. 298–310, 2016.

[9] S. Roy, R. Raju, H. F. Chuang, B. A. Cruden, and M. Meyyappan, "Modeling gas flow through microchannels and nanopores," *Journal of Applied Physics*, vol. 93, no. 8, pp. 4870–4879, 2003.

[10] G. Karniadakis, A. Beskok, and N. Aluru, *Microflows and Nanoflows: Fundamentals and Simulation*, Springer Science Business Media, 2006.

[11] K. Wu, X. Li, C. Wang, W. Yu, and Z. Chen, "Apparent permeability for gas flow in shale reservoirs coupling effects of gas diffusion and desorption," in *Proceedings of the 2nd Unconventional Resources Technology Conference*, pp. 2328–2345, Denver, Colorado, August 2014.

[12] J. Wang, L. Yu, and Q. Yuan, "Experimental study on permeability in tight porous media considering gas adsorption and slippage effect," *Fuel*, vol. 253, pp. 561–570, 2019.

[13] X. Zhang, L. Xiao, X. Shan, and L. Guo, "Lattice Boltzmann simulation of shale gas transport in organic nano-pores," *Scientific Reports*, vol. 4, p. 4843, 2014.

[14] E. Fathi and I. Y. Akkutlu, "Lattice Boltzmann method for simulation of shale gas transport in kerogen," *SPE Journal*, vol. 18, no. 1, pp. 27–37, 2012.

[15] G. A. Bird and J. M. Brady, *Molecular Gas Dynamics and the Direct Simulation of Gas Flows*, Clarendon press, Oxford, 1994.

[16] G. Arya, H. C. Chang, and E. J. Maginn, "Molecular simulations of Knudsen wall-slip: effect of wall morphology," *Molecular Simulation*, vol. 29, no. 10-11, pp. 697–709, 2003.

[17] M. Rahmanian, R. Aguilera, and A. Kantzas, "A new unified diffusion–viscous-flow model based on pore-level studies of tight gas formations," *SPE Journal*, vol. 18, pp. 38–49, 2012.

[18] Y. Li, A. Kalantari-Dahaghi, A. Zolfaghari, P. Dong, S. Negahban, and D. Zhou, "Fractal-based real gas flow model in shales: an interplay of nano-pore and nano-fracture networks," *International Journal of Heat and Mass Transfer*, vol. 127, pp. 1188–1202, 2018.

[19] J. C. Maxwell, "VII. On stresses in rarified gases arising from inequalities of temperature," *Philosophical Transactions of the Royal Society of London*, vol. 170, pp. 231–256, 1879.

[20] Y. Mitsuya, "Modified Reynolds equation for ultra-thin film gas lubrication using 1.5-order slip-flow model and considering surface accommodation coefficient," *Journal of Tribology*, vol. 115, no. 2, pp. 289–294, 1993.

[21] T. Zhao, H. Zhao, X. Li et al., "Pore scale characteristics of gas flow in shale matrix determined by the regularized lattice Boltzmann method," *Chemical Engineering Science*, vol. 187, pp. 245–255, 2018.

[22] T. M. Parfenova, A. E. Kontorovich, L. S. Borisova, and V. N. Melenevskii, "Kerogen from the Cambrian deposits of the Kuonamka Formation (northeastern Siberian Platform)," *Russian Geology and Geophysics*, vol. 51, no. 3, pp. 277–285, 2010.

[23] F. P. Wang, R. M. Reed, A. John, and G. Katherine, "Pore networks and fluid flow in gas shales," in *SPE Annual Technical Conference and Exhibition*, New Orleans, Louisiana, USA, 2009.

[24] C. H. Sondergeld, K. E. Newsham, J. T. Comisky, M. C. Rice, and C. S. Rai, "Petrophysical considerations in evaluating and producing shale gas resources," in *SPE Unconventional Gas Conference*, Pittsburgh, Pennsylvania, USA, 2010.

[25] D. A. Handwerger, D. M. Willberg, M. Pagels, B. Rowland, and J. F. Keller, "Reconciling retort versus dean stark measurements on tight shales," in *SPE Annual Technical Conference and Exhibition*, San Antonio, Texas, USA, 2012.

[26] T. Zhang, X. Li, J. Shi et al., "An apparent liquid permeability model of dual-wettability nanoporous media: a case study of shale," *Chemical Engineering Science*, vol. 187, pp. 280–291, 2018.

[27] A. Vengosh, R. B. Jackson, N. Warner, T. H. Darrah, and A. Kondash, "A critical review of the risks to water resources from unconventional shale gas development and hydraulic fracturing in the United States," *Environmental Science & Technology*, vol. 48, no. 15, pp. 8334–8348, 2014.

[28] F. Javadpour, M. McClure, and M. E. Naraghi, "Slip-corrected liquid permeability and its effect on hydraulic fracturing and fluid loss in shale," *Fuel*, vol. 160, pp. 549–559, 2015.

[29] Q. Wu, B. Bai, Y. Ma, J. T. Ok, K. B. Neeves, and X. Yin, "Optic imaging of two-phase-flow behavior in 1D nanoscale channels," *SPE Journal*, vol. 19, no. 5, pp. 793–802, 2014.

[30] G. R. Chalmers and M. R. Bustin, "PS the Effects and Distribution of Moisture in Gas Shale Reservoir Systems," GR Chalmers, MR Bustin, 2010.

[31] T. Zhao, X. Li, H. Zhao, and M. Li, "Molecular simulation of adsorption and thermodynamic properties on type II kerogen: influence of maturity and moisture content," *Fuel*, vol. 190, pp. 198–207, 2017.

[32] J. Li, X. Li, X. Wang et al., "Water distribution characteristic and effect on methane adsorption capacity in shale clay," *International Journal of Coal Geology*, vol. 159, pp. 135–154, 2016.

[33] J. Li, X. Li, K. Wu, D. Feng, T. Zhang, and Y. Zhang, "Thickness and stability of water film confined inside nanoslits and nanocapillaries of shale and clay," *International Journal of Coal Geology*, vol. 179, pp. 253–268, 2017.

[34] J. Li, X. Li, K. Wu et al., "Water sorption and distribution characteristics in clay and shale: effect of surface force," *Energy & Fuels*, vol. 30, no. 11, pp. 8863–8874, 2016.

[35] K. Wu, Z. Chen, J. Li, X. Li, J. Xu, and X. Dong, "Wettability effect on nanoconfined water flow," *Proceedings of the National Academy of Sciences*, vol. 114, no. 13, pp. 3358–3363, 2017.

[36] Z. Sun, K. Wu, J. Shi et al., "An analytical model for transport capacity of water confined in nanopores," *International Journal of Heat and Mass Transfer*, vol. 138, pp. 620–630, 2019.

[37] J. A. Thomas and A. J. H. McGaughey, "Effect of surface wettability on liquid density, structure, and diffusion near a solid surface," *The Journal of Chemical Physics*, vol. 126, no. 3, article 034707, 2007.

[38] D. Feng, X. Li, X. Wang et al., "Capillary filling of confined water in nanopores: coupling the increased viscosity and slippage," *Chemical Engineering Science*, vol. 186, pp. 228–239, 2018.

[39] K. Wu, Z. Chen, X. Li et al., "Flow behavior of gas confined in nanoporous shale at high pressure: real gas effect," *Fuel*, vol. 205, pp. 173–183, 2017.

[40] J. B. Curtis, "Fractured shale-gas systems," *AAPG Bulletin*, vol. 86, no. 11, pp. 1921–1938, 2002.

[41] T. Zhang, X. Li, J. Li et al., "A fractal model for gas–water relative permeability in inorganic shale with nanoscale pores," *Transport in Porous Media*, vol. 122, no. 2, pp. 305–331, 2018.

[42] D. Chai, Z. Fan, and X. Li, "A new unified gas-transport model for gas flow in nanoscale porous media," *SPE Journal*, vol. 24, no. 2, pp. 698–719, 2019.

[43] A. Goodman, *Imaging Techniques for Analyzing Shale Pores and Minerals*, National Energy Technology Laboratory (NETL), Pittsburgh, PA, Morgantown, WV, and Albany, OR (United States), 2014.

[44] A. Wasaki and I. Y. Akkutlu, "Permeability of organic-rich shale," *SPE Journal*, vol. 20, no. 6, pp. 1384–1396, 2015.

[45] Y. Hu, D. Devegowda, A. Striolo et al., "Microscopic dynamics of water and hydrocarbon in shale-kerogen pores of potentially mixed wettability," *SPE Journal*, vol. 20, no. 1, pp. 112–124, 2014.

[46] A. Jarrahian and E. Heidaryan, "A simple correlation to estimate natural gas viscosity," *Journal of Natural Gas Science and Engineering*, vol. 20, pp. 50–57, 2014.

[47] Q. Zhang, Y. Su, W. Wang, M. Lu, and G. Sheng, "Gas transport behaviors in shale nanopores based on multiple mechanisms and macroscale modeling," *International Journal of Heat and Mass Transfer*, vol. 125, pp. 845–857, 2018.

[48] Z. Sun, X. Li, J. Shi et al., "A semi-analytical model for drainage and desorption area expansion during coal-bed methane production," *Fuel*, vol. 204, pp. 214–226, 2017.

[49] K. Wu, X. Li, C. Wang, Z. Chen, and W. Yu, "A model for gas transport in microfractures of shale and tight gas reservoirs," *AICHE Journal*, vol. 61, no. 6, pp. 2079–2088, 2015.

[50] Q. Zhang, Y. Su, W. Wang, M. Lu, and G. Sheng, "Apparent permeability for liquid transport in nanopores of shale reservoirs: coupling flow enhancement and near wall flow," *International Journal of Heat and Mass Transfer*, vol. 115, pp. 224–234, 2017.

[51] J. K. Holt, H. G. Park, Y. Wang et al., "Fast mass transport through sub-2-nanometer carbon nanotubes," *Science*, vol. 312, no. 5776, pp. 1034–1037, 2006.

[52] Z. Sun, X. Li, J. Shi, T. Zhang, and F. Sun, "Apparent permeability model for real gas transport through shale gas reservoirs considering water distribution characteristic," *International Journal of Heat and Mass Transfer*, vol. 115, pp. 1008–1019, 2017.

[53] A. Beskok and G. E. Karniadakis, "A model for flows in channels, pipes, and ducts at micro and nano scales," *Microscale Thermophysical Engineering*, vol. 3, no. 1, pp. 43–77, 1999.